This document is the accepted manuscript version of the following article:
Piazzese, C., Carminati, M. C., Krause, R., Auricchio, A., Weinert, L., Gripari, P., … Caiani, E. G. (2020). 3D right ventricular endocardium segmentation in cardiac magnetic resonance images by using a new inter-modality statistical shape modelling method. Biomedical Signal Processing and Control, 58, 101866 (11 pp.). https://doi.org/10.1016/j.bspc.2020.101866

3D right ventricular endocardium segmentation in cardiac magnetic resonance images by using a new inter-modality statistical shape modelling method

Concetta Piazzese[1,2], M. Chiara Carminati[3], Rolf Krause[4], Angelo Auricchio[4], Lynn Weinert[5], Paola Gripari[2], Gloria Tamborini[2], Gianluca Pontone[2], Daniele Andreini[2], Roberto M Lang[5], Mauro Pepi[2], Enrico G Caiani[6]

[1] School of Engineering, Cardiff University, Cardiff, United Kingdom
[2] Centro Cardiologico Monzino IRCCS, Milan, Italy
[3] Laboratory for Neutron Scattering and Imaging, Paul Scherrer Institut, Villigen, Switzerland
[4] Center for Computational Medicine in Cardiology, Institute of Computational Science, Università della Svizzera italiana, Lugano, Switzerland
[5] Department of Cardiology, University of Chicago, IL, USA
[6] Dipartimento di Elettronica, Informazione e Bioingegneria, Politecnico di Milano, Italy

Corresponding author:
Concetta Piazzese
School of Engineering, Queen's Buildings, Cardiff University
14-17 The Parade, Cardiff CF24 3AA, United Kingdom
E-mail: concettap@cardiff.ac.uk

Abstract

Objective *Statistical shape modelling (SSM) has established as a powerful method for segmenting the left ventricle in cardiac magnetic resonance (CMR) images However, applying them to segment the right ventricle (RV) is not straightforward because of the complex structure of this chamber. Our aim was to develop a new inter-modality SSM-based approach to detect the RV endocardium in CMR data.*

Methods *Real-time transthoracic 3D echocardiographic (3DE) images of 219 retrospective patients were used to populate a large database containing 4347 3D RV surfaces and train a model. The initial position, orientation and scale of the model in the CMR stack were semi-automatically derived. The detection process consisted in iteratively deforming the model to match endocardial borders in each CMR plane until convergence was reached. Clinical values obtained with the presented SSM method were compared with gold-standard (GS) corresponding parameters.*

Results *CMR images of 50 patients with different pathologies were used to test the proposed segmentation method. Average processing time was 2 minutes (including manual initialization) per patient. High correlations (r^2>0.76) and not significant bias (Bland-Altman analysis) were observed when evaluating clinical parameters. Quantitative analysis showed high values of Dice coefficient (0.87±0.03), acceptable Hausdorff distance (9.35±1.51mm) and small point-to-surface distance (1.91±0.26mm).*

Conclusion *A novel SSM-based approach to segment the RV endocardium in CMR scans by using a model trained on 3DE-derived RV endocardial surfaces, was proposed. This inter-modality technique proved to be rapid when segmenting the RV endocardium with an accurate anatomical delineation, in particular in apical and basal regions.*

Key words: cardiac magnetic resonance images; right ventricular volume; image segmentation; statistical shape model.

1. Introduction

The mayor causes of mortality in Europe are cardiovascular diseases with the 47% of mortality every year [1]. The relationship between the right ventricular function and a number of cardiac diseases (i.e. pulmonary hypertension, congenital heart disease heart failure, myocardial infarction) has been confirmed by different works [2-4]. Correct diagnosis of these pathologies depends on information given by available cardiac imaging modalities. Due to its ability to provide high-quality functional and anatomical images in any anatomical orientation, its ability to modulate tissue contrast in response to several mechanisms and its non-invasiveness [5, 6], cardiac magnetic resonance (CMR) is increasingly used as a standard tool in clinical practice for the evaluation of right ventricle (RV) for. Important clinical parameters, such as volumes, stroke volume (SV) and ejection fraction (EF) are derived by accurate outlining of myocardial contours at end-diastolic (ED) and end-systolic (ES) phase. However, segmenting the RV is a difficult task due to different issues: presence of trabeculations (wall irregularities), dissimilar shape from the apical to basal level, thin and indistinguishable myocardial walls [7, 8]. Consequently, RV border detection is currently performed manually, leading to a tedious and time-consuming task, subject to inter- and intra-observer variability.

In the last decade, several methods have been proposed to automatically or semi-automatically extract cardiac wall borders. More recently, the Right Ventricle Segmentation Challenge [9] attempted to propose a standard framework for the evaluation of the RV segmentation. The results of the challenge, obtained by testing various automatic and semi-automatic detection methods, were summarized and used to address different questions concerning the RV detection (i.e. accuracy to be expected, 2D vs 3D segmentation…).

Statistical shape techniques have become a popular application for medical image segmentation. In this two-step approach, a set of samples is used to train a statistical model (SM) to encode the morphology and the statistical variability of a shape. The trained SM is then applied and deformed to detect the shape in new unseen images. A feature of this approach is that the SM is constrained to deform assuming only acceptable shapes seen in the training set.

Even if model-based approaches (i.e. active shape modelling (ASM) and active appearance modelling (AAM) techniques) have been successfully used to detect LV borders in CMR scans [10-12], a small number of works used model-based techniques to detect RV endocardium [13]. In particular, most of them are based on a joint segmentation of LV and RV taking advantage of the relative positions of the heart chambers and similar grey levels in blood cavities [14-18].

Recently, we developed an inter-modality statistical shape modelling (SSM) approach for segmenting the LV. Briefly, 3D surfaces, obtained from real-time three-dimensional echocardiographic (3DE) data, were used to train the SM [19]. The LV cavity was then detected by applying the SM in CMR short-axis (SAX) and long-axis (LAX) scans [20, 21]. The use of 3DE images allowed to overcome some limitations of previously reported SSM-based techniques and to create a SM:

- with a high statistical power: the power of a SM depends on the number of training samples. In particular, for 3D SMs, the size of the training data is always small due to the difficulty of collecting images and to the long time required to manually segment them. Consequently, in many works present in the literature [10, 22, 23], the SMs are trained on a limited number of samples (less than 100) and characterized by a low power. The high temporal resolution of 3DE imaging allowed us to overcome this limitation and a large quantity of data were available to be used as training samples;
- with a high resolution: the resolution of the SM is defined by the number of its vertices. Training the 3D SM on samples derived from manually traced 2D contours on images with anisotropic resolution (slab thickness several times larger than the planar resolution) and subsequently interpolated along the third dimension [24, 25], reduce the resolution of the SM. On the contrary, the use of training samples derived from 3D surfaces obtained from 3DE data avoided the need of interpolating and allowed to increase the resolution of the SM;
- free from morphological artefacts: training samples are derived from 3DE images that are intrinsically 3D so avoiding potential slice misalignments due to breathing-related motion that could affect the generation of the SM with inaccuracies, such as stair-case aliasing [26, 27];
- with detailed anatomical information of basal and apical regions: a type of information usually not included in the SM [28] due to the problematic visualization of these parts in the 2D CMR SAX images.

Based on these considerations and on the positive results obtained by segmenting LV myocardial contours with the proposed SSM approach [19-21], we assumed a similar inter-modality SSM-based workflow could be developed and used to segment the RV blood cavity from a stack of 2D CMR SAX images. Consequently, in this work, an ad hoc strategy to train a SM on information included in a new database of RV 3D endocardial surfaces is presented, as well as the SSM approach to detect the RV cavity in CMR SAX scans and its validation performed by comparing the obtained results with those derived from the conventional gold-standard (GS) tracing.

2. Materials and Methods

Figure 1 shows an overview of the workflow of the proposed SSM-based method to detect the 3D RV endocardium in CMR SAX images.

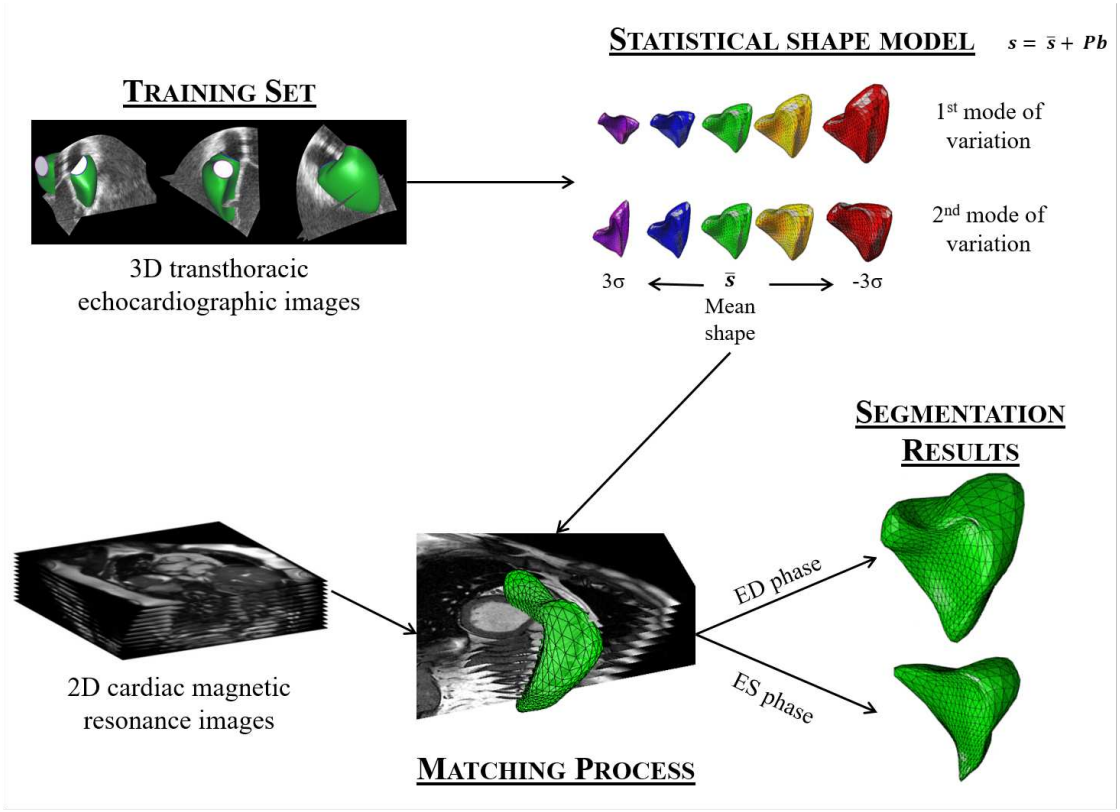

Figure 1. Workflow of the proposed segmentation technique to detect the RV border at ED and ES phase using a 3D SSM-based approach. The SM was trained using a large database containing real-time 3DE data. Segmentation of RV cavities in CMR scans was performed by iteratively deforming the SM using simultaneously the information extracted from the CMR stack of SAX images. At the end of the iteration process, segmentation results are provided as 2D contours on CMR SAX planes or as 3D meshes representing the real expected shape.

2.1 Statistical shape model

2.1.1 Right ventricular shapes collection

A clinical cohort of 219 subjects (mean ± standard deviation (SD): age 51 ± 20 years, range 8 – 99 years, 65 males; ED volume 122 ± 48 ml; ES volume: 70 ± 43 ml; EF: 45 ± 15%; SV: 52 ± 21 ml), including a majority of normal subjects (n = 181) over a wide age range and patients with various pathologies (10 with dilated cardiomyopathy (DCM), 5 with congenital diseases and 23 with mitral valve prolapse) was retrospectively collected. All subjects underwent 3DE examination for clinical reasons at the Centro Cardiologico Monzino, Milano, Italy or University of Chicago, IL, USA In both institutions, wedge-shaped sub-volumes were acquired over 4 to 7 consecutive cardiac cycles during a breath-hold and with ECG gating using Philips iE33 with X3-1 probe. Inclusion criterion was the availability of the segmented 3DE data in the hospital database, with secondary data use approved by IRB in both centres.

For each acquired 3DE data, RV endocardial quantification was performed by using TomTec Image Arena. Following manual initialization of few points, a triangulated mesh, describing the RV endocardium and defined by 1280 faces and 642 vertices, was

automatically exported as a surface for each frame of the cardiac cycle (Figure 1), thus guaranteeing the anatomical correspondences of nodes belonging to each shape. The dataset containing 4347 surfaces corresponding to the RV endocardium, which volumes ranged from 20 ml to 261 ml, was used as set to train the RV SM.

2.1.2 Shapes alignment and dimensionality reduction

The 3D coordinates of the first three vertices (figure 2) in the nodes list corresponding to the position of:

- the pulmonary valve (PV) centre;
- the tricuspid valve (TV) centre;
- the apex (AP).

were automatically extracted for each 3D surface using an in-house developed software.

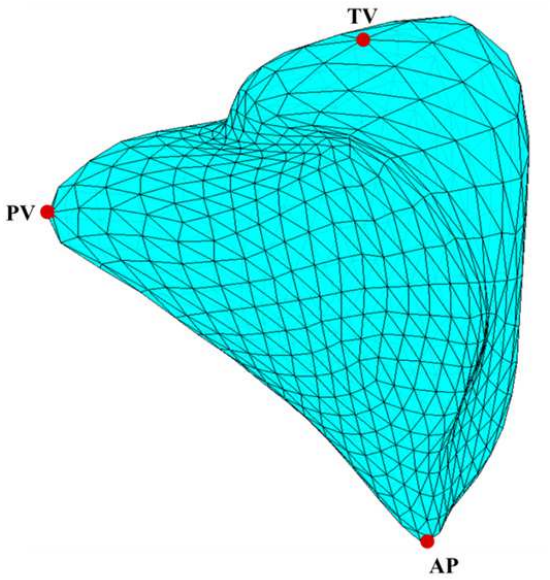

Figure 2. Example of a RV shape semi-automatically obtained from real-time 3D echocardiographic image with a commercial software (Tomtec) and defined by 642 vertices and 1280 faces, with three automatically located fiducial vertices corresponding to RV pulmonary valve (PV), apex (AP) and tricuspid valve (TV) position.

Surface alignment was performed by defining a local reference system as follows:

$$\begin{cases} \mathbf{v_1} = \dfrac{\mathrm{TV} - \mathrm{AP}}{|\mathrm{TV} - \mathrm{AP}|} \\ \mathbf{v_2} = \mathbf{v_1} \times \dfrac{\mathrm{PV} - \mathrm{TV}}{|\mathrm{PV} - \mathrm{TV}|} \\ \mathbf{v_3} = \mathbf{v_1} \times \mathbf{v_2} \end{cases} \quad (1)$$

with $\mathbf{v_1}$ corresponding to the long axis of RV directed from AP to TV, $\mathbf{v_2}$ defined as the orthogonal axis to the plane containing the pulmonary axis $\frac{\mathrm{PV}-\mathrm{TV}}{|\mathrm{PV}-\mathrm{TV}|}$ and $\mathbf{v_1}$, $\mathbf{v_3}$ the orthogonal axis to $\mathbf{v_1}$ and $\mathbf{v_2}$.

Each surface was co-registered to the local reference system of a reference surface randomly chosen (figure 3). To include the anatomical variability of RVs with different dimensions in the SM, scaling was not performed [29].

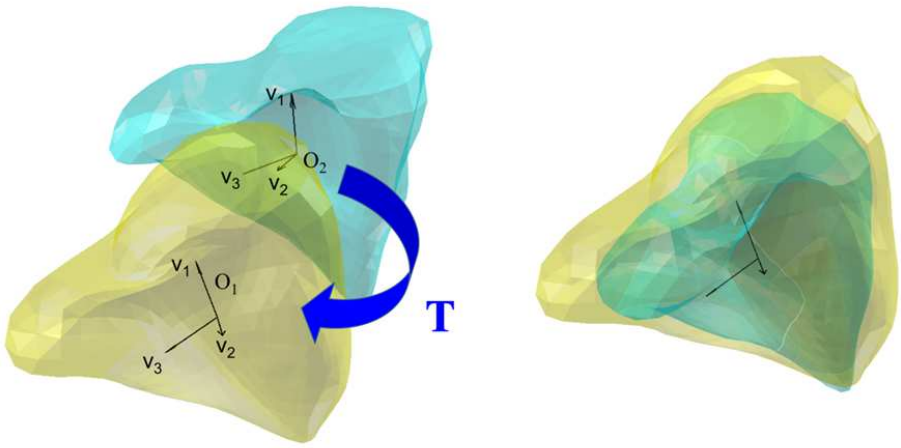

Figure 3. Schematization of the alignment of each training shape, performed by rotating and translating, with a geometric transformation T, the local reference system O_2 (defined by the RV pulmonary valve (PV), the apex (AP) and the tricuspid valve (TV) position) to the local system O_1 of a reference surface.

The database of aligned shapes was analysed through principal component analysis (PCA) to filter and keep only the meaningful information [30]. By averaging the x, y, z coordinates of training surfaces, the mean RV endocardial shape $\bar{\boldsymbol{s}}$ was obtained. Eigenvectors and eigenvalues (λ), representing the principal modes of variation and the variance expressed by each component respectively, were computed from the corresponding covariance matrix so that every valid shape included in the database was approximated as:

$$\boldsymbol{s} = \bar{\boldsymbol{s}} + \boldsymbol{P}\boldsymbol{b} \tag{2}$$

with $\bar{\boldsymbol{s}}$ the mean shape obtained from the samples composing the training set, $\boldsymbol{P}$ the matrix of principal components (PCs) and $\boldsymbol{b}$ the *m*-dimensional vector that holds the shape parameters, limited to $[-3\sqrt{\lambda}, 3\sqrt{\lambda}]$, [31]. Knowing that most of the variance included in the database is explained by a small number of modes, 91 principal modes out of 1926 were retained so to limit the variability explained to 99.73% [32]. Figure 4 shows 2 PCs explaining the highest variance.

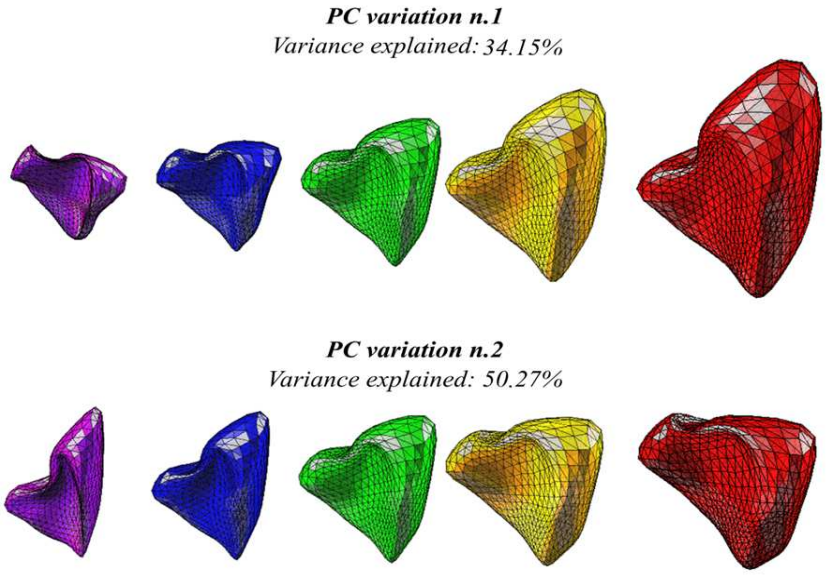

Figure 4. Two PCs and their variations expressed as mean shape – 3√λ (violet), mean shape - 1.5√λ (blu), mean shape (green), mean shape + 1.5√λ (yellow), and mean shape + 3√λ (red) and. The first PC was able to explain 34.15% of the total variance contained in the training set and about 50% when considering the first two PCs.

2.2 CMR images

2.2.1 Population

A total of 50 patients (58 ± 15 years, range 15 – 86 years, 32 males; ED volume: 138 ± 39 ml, ES volume: 66 ± 29 ml, EF: 53 ± 13 %, SV: 73 ± 26 ml) referred for cardiac evaluation at Centro Cardiologico Monzino and diagnosed with ischemic DCM, coronary artery disease (CAD) or normal RV function were retrospectively selected and included in this study (19 CAD, 12 DCM and 19 healthy).

For each patient, CMR 2D SAX and LAX (2-ch, 3-ch and 4-ch views) images were acquired during consecutive apneas with a 1.5T scanner (Discovery MR450, GE Healthcare, Milwaukee, WI, USA) equipped with an eight elements torso coil. The following protocol parameters were used: steady-state free precession (SSFP) gradient echo sequence with retrospective ECG gating, repetition time 3.2 ms, echo time 1.57 ms, no gap between slices, slice thickness 8 mm and pixel size from 0.66 to 0.94 mm.

2.2.2 Pre-processing and manual initialization

Each CMR dataset was visually inspected to select ES and ED frames defined as the ones with RV at minimal and maximal size, respectively. To avoid inaccuracies and distortions in the final RV endocardial SM, the CMR dataset was pre-processed to remove spatial misalignments due to patient's breath-related motion. Both LAX images (2-ch and 4-ch views) were visually assessed in 3D space and their relative position was manually adjusted by applying a 3D translation, if necessary. Then, an automatic

registration corrected each SAX image position with an in-plane translation, optimizing the normalized cross-correlation of intensity profile at the SAX-LAX image intersections [33].

To fit the SM in the CMR SAX stack for segmenting the RV, an initialization step was required. Due to the anisotropic resolution of CMR SAX images and an incorrect inclusion of a SAX planes in the range of scans to be processed, the initialization step was performed by manually selecting anatomical landmarks on LAX planes. In particular, 2 points for TV leaflet insertion (from which the approximate position of TV centre in CMR reference system was obtained) and 1 for RV AP were selected on the 4-ch LAX plane (figure 5 top left). Furthermore, 1 point was placed on the 3-ch LAX image (figure 5 top right) between the RV and the aorta (RA). From these manually placed points, a local reference system for each CMR data was computed similarly as in equation (1) and used to derive the initial pose of the SM in the CMR SAX stack.

The distance between TV and AP was used as apex-to-base distance to scale the initial SM and to automatically select the SAX image of the CMR stack to be segmented. A better definition of the SAX planes range, to be used to guide model deformation, would derive by visually integrating information of a 2-ch LAX image of RV, usually not acquired in clinical practice. For this reason, we developed a 3D interactive visual interface to correct, if necessary, the range of SAX planes to be used for segmentation with a manual correction (figure 5 bottom).

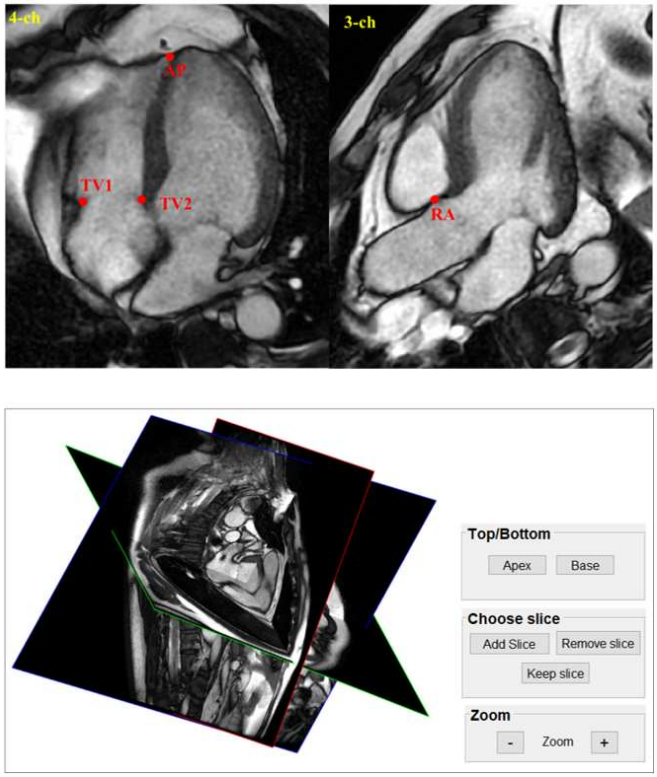

Figure 5. Example of the required manual initialization of four points: three on 4-ch LAX image (top left) corresponding to apex (AP) and tricuspid valve leaflet insertion (TV1 and TV2) and one point on 3-ch LAX plane between the aorta (RA) and the RV (top right). The SAX planes range to be used for model deformation is automatically derived from apex-to-base distance and eventually manual corrected with an interactive visualization tool (bottom).

2.3 RV endocardial segmentation

Prior to the segmentation of the RV endocardium using the proposed approach, a fundamental prerequisite was the detection of the LV myocardium as described in our works [19-21] so to use the resulting 2D contours to exclude the interventricular septum from the RV blood pool detection.

RV endocardium was segmented by iteratively deforming the SM using simultaneously the information extracted from the CMR stack of SAX images. At each iteration, the SM was registered to the stack of selected SAX images (figure 6 top left) and for each mesh triangle crossing a SAX plane, 2 intersection points were obtained (figure 6 top right and bottom). Furthermore, in order to expand the research domain, an additional point was automatically added between the so-obtained points.

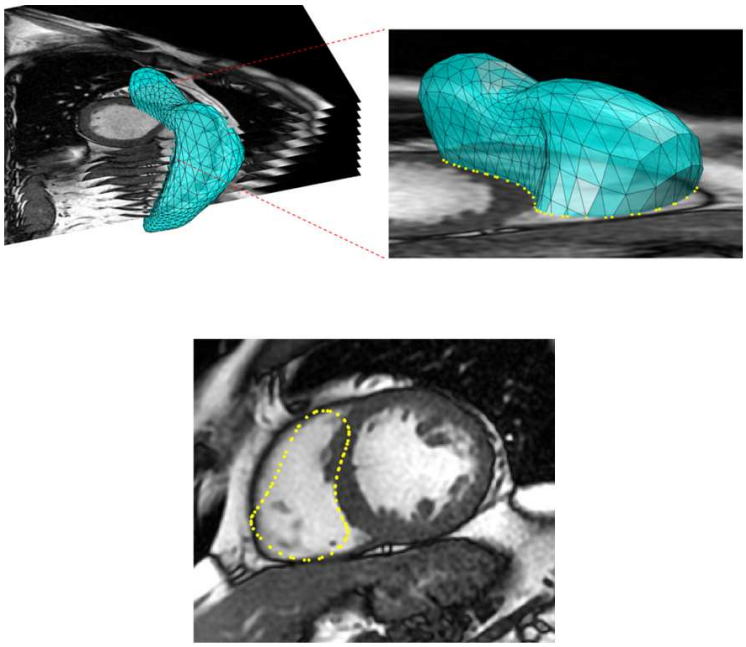

Figure 6. Mean shape registered with the CMR SAX stack of images (top left) and intersections (yellow points) between the SM and a SAX image (top right), resulting in an initial RV endocardial contour on the original 2D plane (bottom).

Due to the tripartite structure of the RV SM that could intersect with basal SAX images generating more than one contour (figure 7 a)), SAX planes with two independently intersected contours (figure 7 b)) were first processed with two Gaussian kernels (figure 7 c)) of different radii (r_1 = 20, r_2 = 7) and σ equal to 100 [7]. In basal SAX images, this step allowed separating the two RV lobes so that each of them could be segmented separately, avoiding possible contours overlapping.

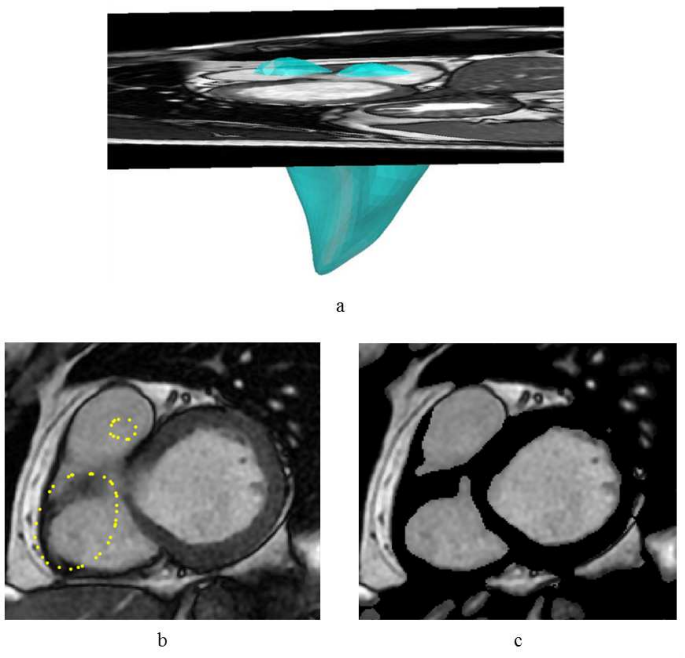

Figure 7. Example of intersection between basal SAX image and the RV SM (a). If more than one intersection contour (yellow points) was detected (b), the image was processed with two Gaussian kernels (c) to segment each of the two RV lobes separately.

To explore surrounding regions, the computed model-image intersections were used, and different searching strategies were exploited due to the semi-lunar profile of the RV on SAX plans. At first iteration, the geometric centre C of all intersections was computed, and the points located on the line connecting each intersection with C were considered (figure 8 a)). For all the remaining iterations, only points lying on the lines normal to the model-image intersection contour were used (figure 8 b) and c)). The former investigation approach allowed a first general scanning of the search space surrounding the computed model-image intersections while the latter permitted to reach insidious regions such as the two extrema points on the interventricular septum junction. In both cases, the length of the line was set to 28 mm for apical SAX images, 32 mm for SAX images at halfway distance between AP and TV and 36 mm for basal SAX images. For basal planes with multiple contours, the space surrounding each curve was investigated separately.

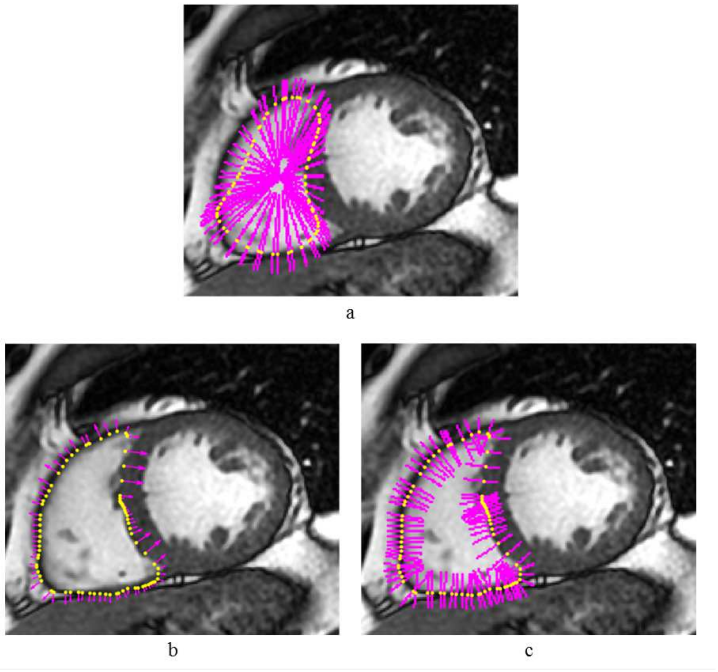

Figure 8. Schematization of different strategies to explore the region surrounding the computed intersections: at the first iteration, lines (magenta) are computed by connecting each intersection point (yellow) to the geometric centre (a); at the second iteration and till the convergence condition is reached, lines (magenta) are computed on the base of the normals to the model-image intersection contour (b and c).

Pixel intensities of the lines obtained were piled up to create a new 2D image L representing the sampled research space (figure 9 a)). The image L does not contain any new information but the extracted pixels in a different format for an easier detection of the RV endocardium. To avoid possible inclusion of LV myocardium, pixels exceeding the interventricular septum were not considered by using information derived from the 2D contours resulting from the LV cavity segmentation with the developed inter-modality SSM approach [19-21].

To distinguish blood pool from other structures, pixels of image L were classified into multiple classes using k-means clustering. The clusters number was determined empirically and was dependent on the location of each SAX image in the stack:

- for apical slices, in which the RV cavity is small and borders less visible, 3 clusters were used to discriminate between blood, myocardium and other structures;
- for basal planes, in which the RV cavity tends to be relatively well-defined and homogenous, 5 clusters (two clusters for blood, three clusters for myocardium and external structures with lower intensities) were used (figure 9 b));
- for middle planes, in which trabeculae are present, 4 clusters were considered (two clusters for blood, two clusters for myocardium and external structures).

The clustered image was thresholded on blood clusters and then binarized. Morphological filters (i.e. closing, filling, exclusion) were applied to eliminate external

structures and isolated pixels so to have white regions representing the RV cavity and black regions representing the myocardium, air and other external structures (figure 9 c)). The RV endocardium (figure 9 d)) was defined as pixels located at the border of the white regions (candidate points) and the corresponding coordinates were transformed back to the CMR reference system.

Procrustes analysis [34] was performed using the detected endocardial features to update the position of the SM in the CMR SAX stack (figure 9 e)). For each vertice of the SM, a weighted displacement vector was obtained. The 3D SM was deformed to match simultaneously the position of the candidate points representing the RV endocardium and the vector **b**, holding shape parameters, was updated. Variation of the SM were restricted to the range $[-3\sqrt{\lambda}, 3\sqrt{\lambda}]$ of the PCs retained during the SM training.

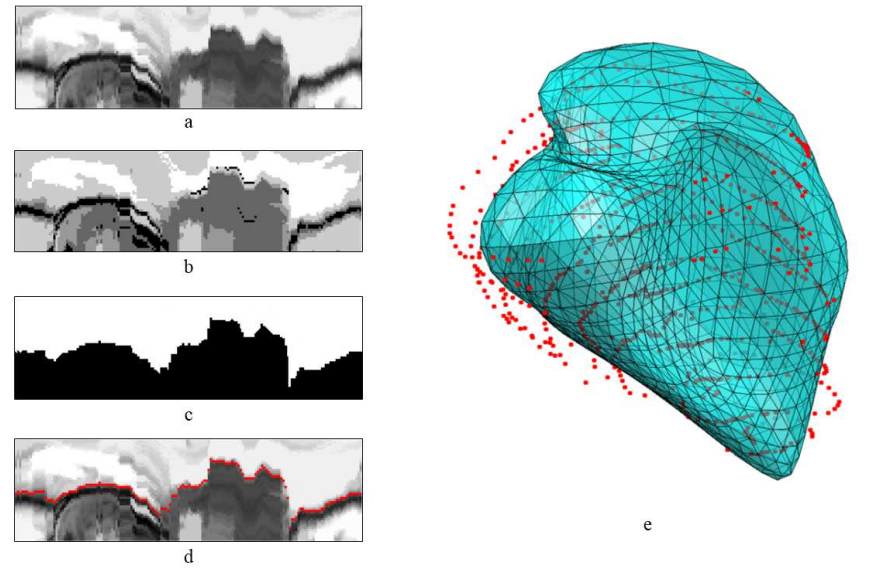

Figure 9. Example of iterative segmentation steps and SM deformation applied to a basal SAX image of the RV: a) intensity Image Created By Combining the grey-level profiles of the computed lines; b) k-means clustering (number of clusters equals to 5); c) binarization by thresholding on blood clusters and removal of external structures to have the white area corresponding to the RV cavity; d) RV endocardial border (red) identified on the initial image; e) positions of the points representing the segmented RV endocardium used to guide the global deformation of the SM.

The deformed model was then re-positioned in the SAX planes and the described segmentation process was iteratively performed, until the displacement of the SM vertices was less than the planar resolution of the SAX images. When this convergence condition was reached, 3D RV volume was computed considering the tetrahedrons composing the 3D RV endocardial mesh.

2.4 Validation protocol

Segmentation accuracy of the proposed approach was assessed on the base of different clinical indices, such as RV endocardial volumes (in ml) at ES and ED phase, EF (in %) and SV (in ml). Bland-Altman analyses and linear regression were applied

between GS and semi-automated derived clinical parameters. To evaluate the significance of the bias, a t-test (paired t-test vs. null values) was performed.

Distance and spatial overlap between 2D contours obtained with the proposed segmentation and manual reference ones were invetigated using Hausdorff distance and Dice similarity. Point-to-surface distance computed as the 3D distance between manual points and the final 3D deformed surface was also evaluated.

3. Results

Segmentation of RV endocardium with the proposed algorithm was performed with an in-house developed software, totally implemented in Matlab (MathWorks). Detection of RV cavity was feasible in all selected patients (feasibility: 100%) and it required a processing time of around 2 minutes (including manual initialization) per patient on a conventional manchine (IntelCore i7, 16 GB RAM, 2.3 GHz). Manual tracing of RV endocardium of an entire stack of CMR SAX slices outlined by an expert operator required around 5 min per frame from which manually derived RV volumes were calculated with the 2D method of discs.

An example of 2D contours obtained segmenting the RV endocardium on ED CMR ECG-triggered images with the proposed approach as well as the resulting 3D surface is shown in figure 10. In particular, it is possible to note in the 4-ch LAX plane the match of the deformed SM to the RV endocardial border especially at apical and basal levels.

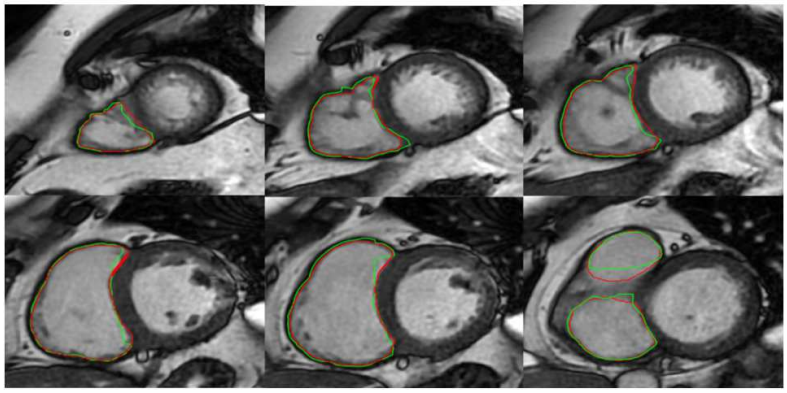

a

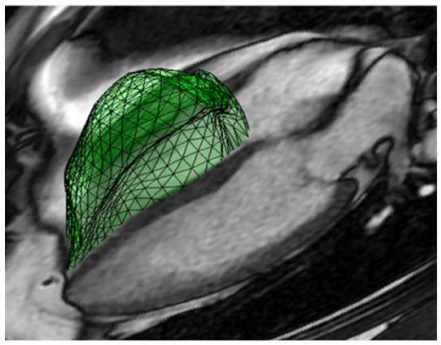

b

Figure 10. Example of the output of the implemented SSM approach: a) 2D semi-automatic contours (green) obtained from the model-image intersections after the converge of the SM with the corresponding 2D contours (red) derived from segmentation; b) 3D RV surface (green) obtained with the proposed approach and the 4-ch LAX plane to better appreciate visualization of apex and base RV morphology.

Correlation analysis of RV volumes (figure 11 top left) showed very high correlation and slopes (r^2 = 0.97, slope = 0.98) compared to the conventional manual GS. A no significant bias of 8.8 ml was found (figure 11 top right) with Bland-Altman analysis. For EF and SV, correlation analysis showed slopes close to 1 but with lower coefficients (EF: slope = 0.98, r^2 = 0.76; SV: slope = 0.89, r^2 = 0.79) when compared to the GS (figure 11 center left and bottom left). Slightly no significant underestimations for EF (bias: -2.4 %) and overestimation for SV (bias: 1.5 ml) derived from 3D volumes were found (figure 11 center right and bottom right) with respect to the GS. For both parameters, acceptable limits of agreements were obtained.

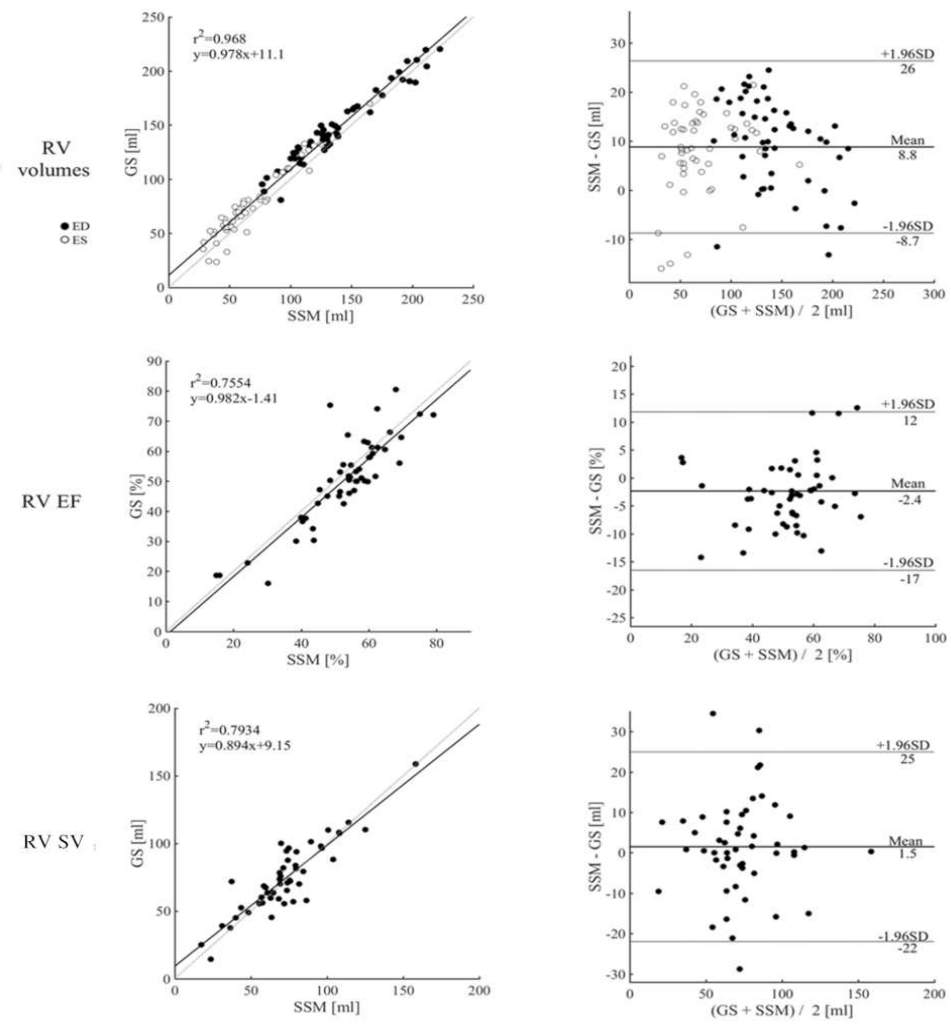

Figure 11. Linear correlations and Bland-Altman analyses of RV volumes (top), EF (centre) and SV (bottom) derived from the GS and the proposed segmentation (SSM).

In table 1, results expressed as mean (SD) of Hausdorff distance, Dice similarity coefficient and point-to surface distance between the manual tracings and the proposed

SSM approach are summarized. Briefly, spatial overlap and distance errors between manual and semi-automatic contours resulted in a Dice coefficient of 0.88 ± 0.03 for ED frame and 0.86 ± 0.03 for ES frame and in a Hausdorff distance of 9.28 ± 1.51 mm and 9.42 ± 1.52 mm for ED and ES frame, respectively. A mean value of 1.91 ± 0.26 mm was obtained when investigating the point-to-surface distance between manual points and the final 3D deformed surface.

Table 1. Dice metric, Hausdorff distance (HD, in mm) and point-to-surface distance (p2s, in mm) for RV endocardium segmentation with the proposed method and other existing detection methods at ES and ED frame. Results are reported as mean (SD).

	Dice		**HD (mm)**		**p2s (mm)**
	ED	**ES**	**ED**	**ES**	**ED and ES**
Proposed method	0.88 (0.03)	0.86 (0.03)	9.28 (1.51)	9.42 (1.52)	1.91 (0.26)
Bai et al. [46]	0.86 (0.11)	0.69 (0.25)	7.70 (3.74)	11.16 (5.53)	-
Zuluaga et al. [41]	0.83 (0.17)	0.72 (0.27)	9.77 (7.88)	11.41 (10.49)	-
Ringenberg et al. [7]	0.88 (0.11)	0.77 (0.18)	7.69 (6.03)	10.71 (7.96)	-
Zhang et al. [15]	-	-	-	-	2.13 (0.39)
Hautvast et al. [49]	-	-	-	-	2.02 (1.21)

4. Discussion

In this work, a new SSM-based method to detect the 3D RV endocardium in CMR SAX images was presented. To the best of our knowledge, this is the first inter-modality SSM-based technique to train a SM on 3D RV endocardial surfaces obtained from 3DE data and apply it to segment the RV endocardium in CMR SAX scans.

The main contributions and findings of this study can be summarized as follow: (a) generation of a SM of the RV using 3D shapes obtained from real-time 3DE data in a representation consistent with the organ of interest; (b) fast and accurate segmentation of healthy and pathological RV cavities in CMR scans with an inter-modality SSM method, requiring a minimal user interaction; (c) segmentation results available as 2D contours on CMR SAX planes or as 3D meshes representing the real expected shape; and (d) a very good correlation of the proposed SSM approach with the manual GS when segmenting the RV endocardium.

Essential requirements of building a SM are the availability of a large training database and knowledge about specific landmarks position on all training shapes. Bai et al. [35] showed that for constructing a SM with a high representative statistical power more than 100 training shapes are required. We achieved all these requirements by training the SM on >4000 3D shapes obtained from semi-automatically segmentation of

transthoracic 3DE images. Since its introduction, 3DE has gained more and more popularity as a reproducible and an accurate imaging method for RV assessment in various conditions [36, 37]. Thanks to different works [38, 39], that provided reference ranges for RV volume and function, 3DE is nowadays used in the everyday clinical practice. Compared to other imaging modalities that can be used to build a SM such as CT [15, 40], 3DE imaging is characterized by higher temporal resolution that allows to obtain a larger number of frames over one cardiac cycle and thus a better selection of the frame at a particular cardiac phase to be included in the training dataset, if needed. It is an imaging modality extensively used in the clinical practice, it is non-invasive, and it has no side effects in subjects with implanted devices or metals in their body. Its low image acquisition cost gives the possibility to easily expand the training set to different patients' groups. Furthermore, compared to CMR, 3DE is intrinsically 3D and quasi-isotropic, thus overcoming the limitation of having a low spatial resolution in the head-to-foot direction, due to the large slice thickness, that implies pixel interpolation to obtain a 3D shape to be used as training sample. Using a training dataset composed by intrinsically and not interpolated 3D surfaces allowed having a SM with an accurate anatomical representation of the RV, in particular at apical and basal levels.

The proposed inter-modality technique proved to be rapid when detecting the RV cavity in CMR SAX scans. A minimal user interaction is required to define the initial pose of the SM in the SAX images to segment. Accordingly, a substantial speedup versus other fully automatic or semi-automatic algorithms was achieved. Zuluaga et al. [41] proposed an accurate coarse-to-fine segmentation strategy in which the RV endocardium segmentation in 2D CMR images is incrementally and automatically updated with a multi-atlas propagation framework. However, that approach resulted to be time-consuming, thus requiring 12 mins to process one patient. Further improvements reduced the computational time up to 45s with the semi–automatic method presented by Grosgeorge et al. [22] in which a manual-derived 2D RV shape is used in a 2D graph cut algorithm with the drawback of a manual selection of 2 points in each image.

Segmentation results with the proposed SSM-based method were available as 2D contours on each plane of the stack of CMR SAX images and as an accurate 3D RV surface in a joint representation with the LV (figure 12). The segmented 2D contours allow computation of important clinical parameters such as volumes, EF or SV using the conventional discs-summation method while the 3D RV mesh could be easily used into a patient-specific finite element model for cardiac electromechanical simulations or surgical planning [42-45].

For all the evaluated clinical parameters a good correlation with the conventional GS was found with the comparison analysis. Acceptable limits of agreement and no significant biases were present when comparing volumes, EF and SV derived from the 3D resulting model to the corresponding GS values. The slight overestimation of RV volumes computed from the 3D deformed model could be justified by the impact of basal and apical regions in the volume computation. These areas are better defined in the 3D model and partially visible if volumes are obtained with the 2D disc integration method.

A comparison of the performance of the proposed approach with previous approaches reported in literature for RV endocardium segmentation is reported in table 1. Our method showed a better accuracy when applying the SM to detect RV endocardium in CMR planes in terms of Hausdorff distance, Dice metric and point-to-surface distance. A slightly higher error in terms of Hausdorff distance was found when assessing the RV endocardium at ED phase in comparison to the study of Ringenberg et al. [7] and Bai et al. [46]. Despite that, according to the results reported from the all compared works [7, 41, 46], the accuracy of RV endocardium segmentation from CMR SAX images in the ED frame was higher than in ES frame. This could be due to the well-defined RV endocardial contour of the ED phase when the RV is more dilated and easier to detected.

Recently, new techniques for the detection of RV endocardium such as graph search or machine leaning algorithms have been presented. In the work of Ghelich Oghli et al. [47], RV region and shape information was incorporated into a livewire framework and used to semi-automatically segment the RV in CMR SAX images. A deep learning algorithm combined with deformable models was proposed by Avendi et al. [48]. However, in both approaches, the segmentation is performed on the 2D CMR SAX images where basal and apical regions are partially visible.

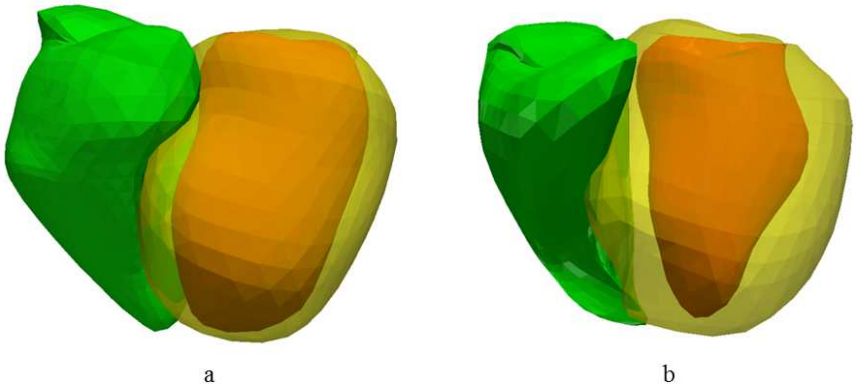

Figure 12. Example of 3D endocardial LV, epicardial LV and endocardial RV meshes (orange, yellow, green, respectively) obtained with the inter-modality SSM approach by sequentially segmenting the CMR images at ED phase (a) or at ES phase (b) of a patient with normal RV function.

An intrinsic limitation of this study is the training database used, mainly composed of patients with normal RV function. However, the SM was successfully employed to detect the RV endocardium in CMR SAX scans of both healthy and pathological patients with promising results. Nevertheless, a further extension of the training database by including more pathological patients could improve the statistical power of the SM as well as the RV endocardium detection performance.

Another limitation is that the SSM approach was applied to CMR images only at ED and ES phase, which are usually utilized to derive global clinical parameters. The possibility to extend the segmentation to all cardiac frames will be further investigated, so to also obtain regional parameters (i.e. regional curves, thickness and local displacement) to assess motion abnormalities of the cardiac wall.

Future improvements consist in reducing the computational time of the RV segmentation process by automatizing the initialization step. For example, the starting pose of the RV SM could be automatically derived from the manually selected points at LV apical and basal levels by taking advantage of the relative position of the ventricular chambers.

In conclusion, we presented a novel inter-modality SSM-based method to detect the RV cavity. Training the model with a dataset composed by 3DE-derived RV endocardial surfaces allowed accurate detection of the RV endocardium in CMR scans especially at apical and basal levels.

Bibliography

1. Nichols M, Townsend N, Scarborough P, Luengo-Fernandez R, Leal J, Gray A, Rayner M. European Cardiovascular Disease Statistics 2012. European Heart Network, Brussels and European Society of Cardiology, Sophia Antipolis, 2012.
2. Matthews JC, Dardas TF, Dorsch MP, Aaronson KD. Right-sided heart failure: diagnosis and treatment strategies. Curr Treat Options Cardiovasc Med. 2008 Aug;10(4):329-41.3
3. de Groote P, Millaire A, Foucher-Hossein C, Nugue O, Marchandise X, Ducloux G, Lablanche JM. Right ventricular ejection fraction is an independent predictor of survival in patients with moderate heart failure. J Am Coll Cardiol. 1998 Oct;32(4):948-54.
4. Mehta SR, Eikelboom JW, Natarajan MK, Diaz R, Yi C, Gibbons RJ, Yusuf S. Impact of right ventricular involvement on mortality and morbidity in patients with inferior myocardial infarction. J Am Coll Cardiol. 2001 Jan;37(1):37-43.
5. Haddad F, Hunt SA, Rosenthal DN, Murphy DJ. Right ventricular function in cardiovascular disease, part I: Anatomy, physiology, aging, and function assessment of the right ventricle. Circulation. 2008 Mar 18;117(11):1436-48.
6. Attili AK, Schuster A, Nagel E, Reiber JHC, van der Geest RJ. Quantification in cardiac MRI: advances in image acquisition and processing. The International Journal of Cardiovascular Imaging. 2010;26(Suppl 1):27-40.
7. Ringenberg J, Deo M, Devabhaktuni V, Berenfeld O, Boyers P, Gold J. Fast, accurate, and fully automatic segmentation of the right ventricle in short-axis cardiac MRI. Computerized Medical Imaging and Graphics, Volume 38(3):190-201, 2014.
8. Grosgeorge D, Petitjean C, Dacher JN, Ruan S. Graph cut segmentation with a statistical shape model in cardiac MRI. Computer Vision and Image Understanding, 117(9): 1027-1035, 2013.
9. Petitjean C, Zuluaga MA, Bai W, Dacher JN, Grosgeorge D, Caudron J, Ruan S, Ayed IB, Cardoso MJ, Chen HC, Jimenez-Carretero D, Ledesma-Carbayo MJ, Davatzikos C, Doshi J, Erus G, Maier OM, Nambakhsh CM, Ou Y, Ourselin S, Peng CW, Peters NS, Peters TM, Rajchl M, Rueckert D, Santos A, Shi W, Wang CW, Wang H, Yuan J. Right ventricle segmentation from cardiac MRI: a collation study. Med Image Anal. 2015 Jan;19(1):187-202.
10. van Assen HC, Danilouchkine MG, Dirksen MS, Reiber JH, Lelieveldt BP. A 3-D active shape model driven by fuzzy inference: application to cardiac CT and MR. IEEE Trans Inf Technol Biomed. 2008 Sep;12(5):595-605.
11. Andreopoulos A, Tsotsos JK. Efficient and generalizable statistical models of shape and appearance for analysis of cardiac MRI. Med. Image Anal. 12 (3), 335–357, 2008.
12. Lekadir K, Merrifield R, Yang GZ. Outlier detection and handling for robust 3-D active shape models search. IEEE Trans Med Imaging 26(2):212–222, 2007.

13. Piazzese C, Carminati MC, Pepi M, Caiani EG. Statistical Shape Models of the Heart: Applications to Cardiac Imaging. Chapter 16 in Statistical Shape and Deformation Analysis, Academic Press, 2017, Pages 445-480.
14. Lötjönen JM, Järvinen VM, Cheong B, Wu E, Kivistö S, Koikkalainen JR, Mattila JJ, Kervinen HM, Muthupillai R, Sheehan FH, Lauerma K. Evaluation of cardiac biventricular segmentation from multiaxis MRI data: a multicenter study. J Magn Reson Imaging. 2008 Sep;28(3):626-36.
15. Zhang H, Wahle A, Johnson RK, Scholz TD, Sonka M. 4-D cardiac MR image analysis: left and right ventricular morphology and function. IEEE Trans Med Imaging. 2010 Feb;29(2):350-64.
16. Mitchell SC, Lelieveldt BP, van der Geest RJ, Bosch HG, Reiber JH, Sonka M. Multistage hybrid active appearance model matching: segmentation of left and right ventricles in cardiac MR images. IEEE Trans Med Imaging. 2001 May;20(5):415-23.
17. Lorenz C, von Berg J. A comprehensive shape model of the heart. Med Image Anal, 2006.
18. Ecabert O, Peters J, Schramm H, Lorenz C, von Berg J, Walker MJ, Vembar M, Olszewski ME, Subramanyan K, Lavi G, Weese J. Automatic model-based segmentation of the heart in CT images. IEEE Trans Med Imaging, Sep;27(9):1189-201, 2008.
19. Piazzese C, Carminati MC, Colombo A, Krause R, Potse M, Auricchio A, Weinert L, Tamborini G, Pepi M, Lang RM, Caiani EG. Segmentation of the left ventricular endocardium from magnetic resonance images by using different statistical shape models. J Electrocardiol. 2016 May-Jun;49(3):383-91.
20. Caiani EG, Colombo A, Pepi M, Piazzese C, Maffessanti F, Lang RM, Carminati MC. Three-dimensional left ventricular segmentation from magnetic resonance imaging for patient-specific modelling purposes. Europace. 2014 Nov;16 Suppl 4:iv96-iv101.
21. Carminati MC, Piazzese C, Pepi M, Tamborini G, Gripari P, Pontone G, Krause R, Auricchio A, Lang RM, Caiani EG. A statistical shape model of the left ventricle from real-time 3D echocardiography and its application to myocardial segmentation of cardiac magnetic resonance images. Comput Biol Med. 2018 May 1;96:241-251.
22. Grosgeorge D, Petitjean C, Ruan S, Caudron J, Dacher J-N. Right ventricle segmentationby graph cut with shape prior. In: Workshop in medical image computing and computer assisted intervention. 2012.
23. Albà X, Pereañez M, Hoogendoorn C, Swift AJ, Wild JM, Frangi AF, Lekadir K. An algorithm for the segmentation of highly abnormal hearts using a generic statistical shape model. IEEE transactions on medical imaging, 2016, 35.3: 845-859.
24. Lamata P, Cookson A, Smith N. Clinical Diagnostic Biomarkers from the Personalization of Computational Models of Cardiac Physiology. Ann Biomed Eng. 2016 Jan;44(1):46-57.

25. Santiago C, Nascimento JC, Marques JS. A new ASM framework for left ventricle segmentation exploring slice variability in cardiac MRI volumes. Neural Computing and Applications, 1-12, 2016.
26. Medrano-Gracia P, Cowan BR, Bluemke DA, Finn JP, Lima JA, Suinesiaputra A, Young AA. Large scale left ventricular shape atlas using automated model fitting to contours. In International Conference on Functional Imaging and Modeling of the Heart, pp. 433-441, Springer Berlin Heidelberg, 2013.
27. Böhler T, Boskamp T, Müller H, Hennemuth A, Peitgen HO. Evaluation of Active Appearance Models for Cardiac MRI. In Bildverarbeitung für die Medizin, pp. 171-175, Springer Berlin Heidelberg, 2006.
28. Su Y, Tan ML, Teo SK, Lim CW, Zhong L, Tan RS. Automatic generation of surface meshes for right ventricle with 1-to-1 correspondence from cine-MR images. In Computing in Cardiology Conference (CinC), pp. 753-756, 2015.
29. Humphries SM, Hunter KS, Shandas R, Deterding RR, DeBoer EM. Analysis of pediatric airway morphology using statistical shape modeling. Med Biol Eng Comput. 2016 Jun;54(6):899-911.
30. Jolliffe I. Principal Component Analysis. John Wiley & Sons, Ltd, 2002.
31. Cootes TF, Taylor CJ, Cooper DH, Graham J. Active shape models – their training and application. Comput. Vis. Image Und., 61 (1), pp. 38–59, 1995.
32. Cootes TF, Taylor CJ. Statistical models of appearance for computer vision. Technical report, University of Manchester, Wolfson Image Analysis Unit, Imaging Science and Biomedical Engineering, Manchester M13 9PT, United Kingdom, 2004. Report available from http://www.isbe.man.ac.uk/bim/refs.html.
33. Carminati MC, Maffessanti F, Caiani EG. Nearly automated motion artifacts correction between multi breath-hold short-axis and long-axis cine CMR images. Comput Biol Med. 2014 Mar;46:42-50.
34. Gower J. Generalized Procrustes analysis. Psychometrika 1975;40:33–51.
35. Bai W, Shi W, de Marvao A, Dawes TJ, O'Regan DP, Cook SA, Rueckert D. A bi-ventricular cardiac atlas built from 1000+ high resolution MR images of healthy subjects and an analysis of shape and motion. Med Image Anal. 2015 Sep 1;26(1):133-145.
36. Fusini L, Tamborini G, Gripari P, Maffessanti F, Mazzanti V, Muratori M, Salvi L, Sisillo E, Caiani EG, Alamanni F, Fiorentini C, Pepi M. Feasibility of intraoperative three-dimensional transesophageal echocardiography in the evaluation of right ventricular volumes and function in patients undergoing cardiac surgery. J Am Soc Echocardiogr. 2011 Aug;24(8):868-77.
37. Grewal J, Majdalany D, Syed I, Pellikka P, Warnes CA. Three-dimensional echocardiographic assessment of right ventricular volume and function in adult patients with congenital heart disease: comparison with magnetic resonance imaging. J Am Soc Echocardiogr. 2010 Feb;23(2):127-33.
38. Tamborini G, Marsan NA, Gripari P, Maffessanti F, Brusoni D, Muratori M, Caiani EG, Fiorentini C, Pepi M. Reference values for right ventricular volumes and ejection fraction with real-time three-dimensional echocardiography: evaluation in a large series of normal subjects. J Am Soc Echocardiogr. 2010 Feb;23(2):109-15.

39. Maffessanti F, Muraru D, Esposito R, Gripari P, Ermacora D, Santoro C, Tamborini G, Galderisi M, Pepi M, Badano LP. Age-, body size-, and sex-specific reference values for right ventricular volumes and ejection fraction by three-dimensional echocardiography: a multicenter echocardiographic study in 507 healthy volunteers. Circ Cardiovasc Imaging. 2013 Sep;6(5):700-10.
40. Hoogendoorn C, Duchateau N, Sanchez-Quintana D, Whitmarsh T, Sukno FM, De Craene M, Lekadir K, Frangi AF. A high-resolution atlas and statistical model of the human heart from multislice CT. IEEE Transactions on Medical Imaging, 32(1):28–44, 2013.
41. Zuluaga MA, Cardoso MJ, Ourselin S. Automatic right ventricle segmentation using multi-label fusion in cardiac MRI. In: Workshop in medical image computing and computer assisted intervention. 2012.
42. Xia L, Huo MM, Wei Q, Liu F, Crozier S. Analysis of cardiac ventricular wall motion based on a three.-dimensional electromechanical biventricular model. Phys. Med. Biol., vol. 50, pp.1901 -1917 2005.
43. Lopez-Perez A, Sebastian R, Ferrero JM. Three-dimensional cardiac computational modelling: methods, features and applications. BioMedical Engineering OnLine. 2015;14:35. doi:10.1186/s12938-015-0033-5.
44. Wenk JF, Zhang Z, Cheng G, Malhotra D, Acevedo-Bolton G, Burger M, Suzuki T, Saloner DA, Wallace AW, Guccione JM, Ratcliffe MB. First finite element model of the left ventricle with mitral valve: insights into ischemic mitral regurgitation. Ann Thorac Surg, May, 89(5):1546-53, 2010.
45. de Vecchi A, Gomez A, Pushparajah K, Schaeffter T, Simpson JM, Razavi R, Penney GP, Smith NP, Nordsletten DA. A novel methodology for personalized simulations of ventricular hemodynamics from noninvasive imaging data. Comput Med Imaging Graph, Jul;51:20-31, 2016.
46. Bai W, Shi W, Wang H, Peters NS, Rueckert D. Multi-atlas based segmentation with local label fusion for right ventricle MR images. In: Proceedings of MICCAI RV segmentation challenge, 2012.
47. Ghelich Oghli M, Mohammadzadeh A, Kafieh R, Kermani S. A hybrid graph-based approach for right ventricle segmentation in cardiac MRI by long axis information transition. Phys Medica 2018;54.
48. Avendi MR, Kheradvar A, Jafarkhani H. Automatic segmentation of the right ventricle from cardiac MRI using a learning-based approach. Magn Reson Med, 78(6):2439-2448, 2017.
49. Hautvast G, Lobregt S, Breeuwer M, Gerritsen F. Automatic contour propagation in cine cardiac magnetic resonance images. IEEE Trans Med Imaging, 25(11):1472-82, 2006.